An extended halo around an ancient dwarf galaxy

Anirudh Chiti [1] ✉, Anna Frebel [1], Joshua D. Simon[2], Denis Erkal[3], Laura J. Chang[4], Lina Necib[2], Alexander P. Ji[2], Helmut Jerjen[5], Dongwon Kim[6] and John E. Norris[5]

The Milky Way is surrounded by dozens of ultrafaint ($<10^5 L_\odot$) dwarf satellite galaxies[1–3]. They are the remnants of the earliest galaxies[4], as confirmed by their ancient[5] and chemically primitive[6,7] stars. Simulations[8–10] suggest that these systems formed within extended dark matter halos and experienced early galaxy mergers and feedback. However, the signatures of these events would lie outside their core regions[11], where spectroscopic studies are challenging[12]. Here we identify members of the Tucana II ultrafaint dwarf galaxy out to nine half-light radii, demonstrating the system to be markedly more spatially extended and chemically primitive than previously found. The distant stars in this galaxy are, on average, extremely metal poor ($\lesssim 1/1000$ of the solar iron abundance), affirming Tucana II as the most metal-poor known galaxy. We observationally establish an extended dark matter halo surrounding an ultrafaint dwarf galaxy out to 1 kpc, with a total mass of $>10^7 M_\odot$, consistent with a generalized Navarro–Frenk–White density profile. The extended nature of Tucana II suggests that it may have undergone strong bursty feedback or been the product of an early galactic merger[10,11]. We demonstrate that spatially extended stellar populations in ultrafaint dwarf galaxies[13,14] are observable, opening up the possibility for detailed studies of the stellar halos of relic galaxies.

Tucana II is a typical ultrafaint dwarf galaxy: it is extremely dark matter dominated (mass/luminosity, $M/L \approx 2{,}000$; ref. [15]), has a low metallicity ($\langle[\text{Fe/H}]\rangle = -2.7$; refs. [16,17]) and has a low stellar mass ($\sim 3{,}000\, M_\odot$; ref. [18]). As with similar systems[3], spectroscopy of its member stars remains sparse due to its low stellar density[18,19]. Previous follow-up spectroscopic studies were largely limited to stars within two half-light radii[15–17] and identified ten probable members of Tucana II.

To substantially extend the spectroscopic characterization of Tucana II, we obtained wide-field images ($\sim 2° \times 2°$) with the Australian National University (ANU) 1.3 m SkyMapper telescope[20] and used its unique filter-set to efficiently identify metal-poor red giant stars at large galactocentric distances[21]. This efficiency arises because the filter-set enables the derivation of stellar metallicity and surface gravity solely from photometry. By combining these derived stellar parameters with Gaia Data Release 2 (DR2) proper motions[22], we identified new candidate member stars in Tucana II in a spatially unbiased manner (Extended Data Figs. 1 and 2). We then verified their membership and spectroscopically characterized nine of these stars, nearly doubling the previously known stellar population of this galaxy. These stars were detected out to about nine times the half-light radius[18] (~1 kpc) of Tucana II, far beyond member stars in other ultrafaint dwarf galaxies, which have not been detected beyond

about four half-light radii. A colour–magnitude diagram of our observed stars and sample spectra is shown in Extended Data Fig. 3.

Our follow-up spectroscopic observations of candidate members were performed with the Magellan Echellette (MagE) Spectrograph[23] and Inamori-Magellan Areal Camera and Spectrograph (IMACS)[24] instruments on the 6.5 m Magellan Baade telescope.

These spectra enable measurement of radial velocities with precisions of $\sim 3\,\text{km s}^{-1}$ and $\sim 1\,\text{km s}^{-1}$, respectively, and metallicities with precisions of ~0.2 to ~0.3 dex. Such precisions are sufficient to conclusively determine the membership status of all candidate stars from a joint velocity and metallicity analysis. The metallicities of our confirmed Tucana II members observed with MagE are presented in Table 1. Detailed summaries of the MagE observations, velocities and metallicities are in Supplementary Tables 1, 2 and 3, respectively.

The metallicities of the spatially extended members decrease the Tucana II galactic metallicity to $\langle[\text{Fe/H}]\rangle = -2.77$, affirming Tucana II as the most metal-poor galaxy known. Metallicities from previous work[16,17] already showed Tucana II to have a low average metallicity of $\langle[\text{Fe/H}]\rangle = -2.71$. However, we find that the stars beyond two half-light radii are preferentially more metal poor ($\langle[\text{Fe/H}]\rangle = -3.02$) than the already studied core population (Fig. 1), which has a mean metallicity of ($\langle[\text{Fe/H}]\rangle = -2.62$). Such metallicity differentials have previously been seen in larger dwarf galaxies and are hypothesized to result from, for example, chemical evolution, feedback or mergers[25]. Our finding provides tentative evidence of such behaviour in a relic early galaxy, indicating that their formation may have also been shaped by the same processes.

The spatial configuration of Tucana II members—12 giants within two half-light radii and seven between two and nine half-light radii—suggests that this ultrafaint dwarf galaxy's stellar density profile may differ from one typically assumed for such systems. Under the common assumption of an exponential density profile, we would not statistically expect to see seven giant stars beyond about two half-light radii (~0.24 kpc; ref. [18]) in a sample of 19 members. However, when assuming a Plummer profile, it is unlikely but still plausible in principle (at a 7% level) to identify seven giant stars beyond about two half-light radii in a sample of 19 members. Conclusive results rest on a precise knowledge of the half-light radius, which is currently not well constrained (Methods). Deeper photometry and more precise structural parameters of Tucana II would thus enable a more robust determination of these potential density profile differences. Any such discrepancies might cause concern regarding the existence of these distant members in Tucana II, but with the possible exception of the most metal-rich star (Methods) every distant star is unambiguously a member. We expect no false positive classifications among our most metal-poor

[1]Department of Physics & Kavli Institute for Astrophysics and Space Research, Massachusetts Institute of Technology, Cambridge, MA, USA. [2]Observatories of the Carnegie Institution for Science, Pasadena, CA, USA. [3]Department of Physics, University of Surrey, Guildford, UK. [4]Department of Physics, Princeton University, Princeton, NJ, USA. [5]Research School of Astronomy and Astrophysics, Australian National University, Canberra, Australian Capital Territory, Australia. [6]Department of Astronomy, University of California, Berkeley, Berkeley, CA, USA. ✉e-mail: achiti@mit.edu

Table 1 | Tucana II member stars observed with MagE

Name	RA (h:min:s)	Dec. (°:':")	g	$g-i$	RV_{hel} (km s^{-1})	σ_{rv} (km s^{-1})	[Fe/H]	$\sigma_{[Fe/H]}$
Tuc2-301	22:50:45.097	−58:56:20.483	18.87	0.57	−128.0	3.3	−3.31	0.18
Tuc2-303	22:53:05.194	−57:54:27.032	18.44	0.54	−130.0	3.5	−2.76	0.25
Tuc2-305	22:57:46.859	−57:43:39.299	18.47	0.60	−124.5	3.1	−3.50	0.17
Tuc2-306	22:51:37.019	−58:53:37.579	18.38	0.67	−120.2	3.1	−3.12	0.17
Tuc2-309	22:49:24.690	−58:20:47.429	18.73	0.63	−133.8	3.1	−1.96	0.18
Tuc2-310	22:52:47.376	−58:46:04.102	19.12	0.44	−124.6	3.5	−2.73	0.20
Tuc2-318	22:51:08.309	−58:33:08.129	18.47	0.60	−129.1	3.1	−2.62	0.20
Tuc2-319	22:52:32.722	−58:36:30.488	19.33	0.58	−123.0	3.3	−2.24	0.21
Tuc2-320	22:51:00.921	−58:32:14.118	19.28	0.49	−115.6	3.2	−2.70	0.18
Tuc2-321	22:52:21.380	−58:31:07.356	19.42	0.47	−123.3	3.3	−2.67	0.21

MagE metallicities and velocities of Tucana II member stars. The right ascension (RA) and declination (dec.) columns indicate the coordinates. g are SkyMapper magnitudes and $g-i$ are extinction-corrected SkyMapper colours. RV_{hel} lists the heliocentric radial velocity and [Fe/H] the metallicity of each star, together with their associated uncertainties.

distant stars because the systemic velocity (−129.1 km s^{-1}) and low mean metallicity ($\langle$[Fe/H]$\rangle \approx -2.77$) of Tucana II are well separated from those of foreground Milky Way stars (Methods and Extended Data Fig. 4).

Tidal disruption is the most obvious process to displace stars to large radii, but that explanation is inconsistent with the orbital parameters of Tucana II (Methods). The location of any predicted Tucana II tidal debris, on the basis of its orbit, would be perpendicular to the position of the most distant newly discovered Tucana II member stars (Fig. 1). Furthermore, tidally disrupted systems should display a velocity gradient[26], which is not observed in Tucana II. For instance, the radial velocity of the farthest star, at 9.3 half-light radii, is only ~1 ± 3 km s^{-1} away from the systemic velocity of Tucana II. Therefore, Tucana II is currently not tidally disrupting.

It follows that the farthest star in Tucana II must be gravitationally bound to the system, given that Tucana II is not tidally disrupting and that the probability of falsely identifying a member is negligible (Methods). To be bound, the farthest star must lie within the tidal radius of Tucana II. Thus, the tidal radius of Tucana II must extend beyond 1 kpc, which requires an enclosed total mass within 1 kpc of at least $1.3 \times 10^7 M_\odot$ (Methods). This mass is a factor of 4 larger than the mass within one half-light radius. Such extended, massive dark matter halos of relic galaxies were predicted[27], but previous mass estimates of ultrafaint dwarf galaxies were limited to those within a few hundred parsecs. Our study confirms that the halo of a relic galaxy contains substantial mass out to a large distance (~1 kpc). The majority of this extended mass distribution of at least $1.3 \times 10^7 M_\odot$ must consist of dark matter, given the low stellar mass of Tucana II (~3,000 $M_\odot$; ref. [18]).

We estimate the mass for this extended dark matter halo by attempting to directly model Tucana II with a generalized Navarro–Frenk–White (NFW) dark matter density profile. This mass enclosed within about nine half-light radii comes to $(2.2^{+4.4}_{-1.3}) \times 10^7 M_\odot$. At face value, this estimate is in excellent agreement with the mass deduced from assuming that the farthest member star is bound and thus adds further evidence that these distant stars are indeed bound to Tucana II. We note that adopting the highest and lowest plausible velocity anisotropy prescriptions only varies this mass at the ~1σ level (Methods). We show the corresponding enclosed mass and density profiles of Tucana II in Fig. 2. To test whether masses at large radii can be extrapolated from estimates within the half-light radius, we also calculated the NFW density profile solely from previously known members[15] and extrapolated to about nine half-light radii. This extrapolation results in a consistent enclosed mass as inferred from all member stars, and supports the common prac-

tice of extrapolating the masses from within one half-light radius to larger radii to, for instance, compare with theoretical models[27]. We also note that our derived mass within 1 kpc of ~$2 \times 10^7 M_\odot$ is consistent with an overall halo mass of ~$10^8 M_\odot$, roughly compatible with constraints on the minimum virial halo mass[28].

As previously noted, our more distant member stars tend to have lower metallicities than those in the galaxy core (see Methods for a full discussion). If such behaviour were to exist in other ultrafaint dwarf galaxies, then the dwarf galaxy metallicities derived only from core populations may be biased high. This bias might affect previous studies that place ultrafaint dwarf galaxies on the dwarf galaxy mass–metallicity relation, a key prediction from galaxy formation simulations that is sensitive to mechanisms including supernova yields, feedback and gas accretion[29]. For instance, lowering the mean metallicity of the most metal-poor ultrafaint dwarf galaxies may increase the number of plausible feedback prescriptions in simulating these systems[29].

One way to form the extended stellar halo component of Tucana II is by heating the system via galaxy mergers or stellar feedback. This interpretation implies Tucana II to be the product of an early merger, probably that of two primitive galaxies at high redshift ($z \gtrsim 2$)[8]. Simulations do indeed suggest that a dwarf galaxy with the stellar mass of Tucana II (~3,000 $M_\odot$; ref. [18]) should be assembled by no more than a handful of star-forming progenitors[30]. Otherwise, early supernova feedback may have heated the most metal-poor stars, which is plausible since ultrafaint dwarf galaxies may have a bursty star formation history[10].

Our detection of a population of stars out to about nine half-light radii in Tucana II suggests that other ultrafaint dwarf galaxies could plausibly host member stars at large radii as well. Indeed, the ultrafaint dwarf galaxies Segue 1 and Bootes I currently each have one known member star at about four half-light radii[13,14]. With targeted wide-field photometric searches, it should be feasible to rapidly uncover the distant members of Segue 1, Bootes I and additional dwarf galaxies to comprehensively establish the evolution of these early relic systems.

Methods

Selection of candidate members. Targets were initially selected using deep narrow-band imaging of the Tucana II ultrafaint dwarf galaxy obtained using the 1.3 m SkyMapper telescope at Siding Springs Observatory[20] between July and December 2015. The SkyMapper filter-set[31] is unique in that the flux through the u, v, g and i filters can be related to stellar metallicity and surface gravity[31,32,33]. Therefore, SkyMapper photometry can directly identify metal-poor red giant stars. These stars are more likely to be members of the Tucana II ultrafaint dwarf galaxy, since the mean metallicity of Tucana II is very low ($\langle$[Fe/H]$\rangle \approx -2.7$;
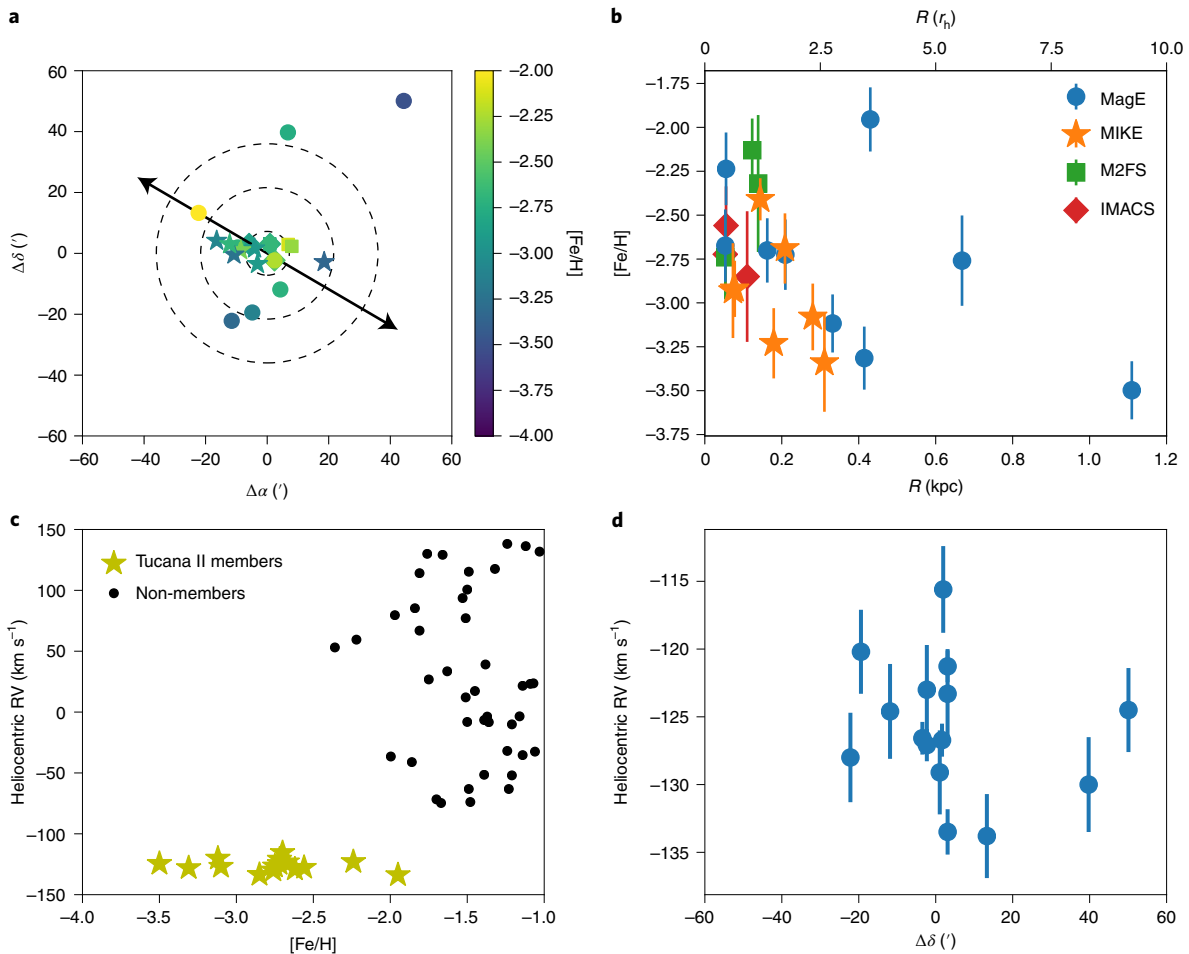
Fig. 1 | Spatial, radial velocity and metallicity distributions of Tucana II stars. a, Spatial distribution of all confirmed member stars of the Tucana II ultrafaint dwarf galaxy, coloured by metallicity. The dashed ellipses correspond to one, three and five half-light radii[18]. Metallicities from Magellan Inamori Kyocera Echelle (MIKE) high-resolution spectra are shown as stars[17], those from Michigan/Magellan Fiber Spectrograph (M2FS) spectra are squares[15] and those from MagE and IMACS spectra presented in this work are circles and diamonds, respectively. For Tucana II stars with no high-resolution MIKE results, we plot all our available medium-resolution measurements. Metallicities from M2FS spectra are reduced by 0.32 dex for agreement with high-resolution metallicities (Methods). Arrows indicate the direction of predicted Tucana II tidal debris (Methods). **b**, Metallicities of Tucana II member stars as a function of their geometric radius *R* from the centre of the system. r_h, half-light radius. As for **a**, metallicities from M2FS spectra are reduced by 0.32 dex. The error bars correspond to 1σ uncertainties on the metallicity, as derived in the Methods. **c**, Heliocentric radial velocities and metallicities of our IMACS and MagE Tucana II members (yellow stars), compared with non-members in those samples with metallicity measurements, and non-members with signal-to-noise ratio (S/N) > 5 observed with M2FS[15] (black circles). **d**, Heliocentric radial velocities from MagE and IMACS measurements of Tucana II members as a function of distance (dec.) from the centre of the system. The error bars correspond to 1σ uncertainties on the velocity measurements, as derived in the Methods.

refs. [16,17]) compared with most Milky Way halo stars, and on the basis of the distance of Tucana II all members brighter than $g \approx 22$ should be red giant stars or blue horizontal branch stars[18,19].

In previous work[21], we have shown that stellar metallicities and surface gravities can be quantitatively determined from SkyMapper photometry by generating synthetic photometry[34,35] over a range of stellar parameters and relating observed magnitudes to theoretical magnitudes from this synthetic grid. We applied this method to derive surface gravities and metallicities for every star brighter than $g \approx 19.5$ in the field of view of the SkyMapper telescope (~2° × ~2°). We thereby identified many metal-poor ($[Fe/H] < -1.0$) giant ($\log g < 3.0$) stars as candidate members of Tucana II.

We further refined this sample of likely member stars by making use of Gaia DR2 proper motion data[22,36]. Since ultrafaint dwarf galaxies are gravitationally bound, their member stars should have proper motions clustered around the systemic proper motion of the galaxy. We narrowed down our sample of candidates by only including stars with proper motions close to the systemic proper motion of Tucana II ($\mu_\alpha \cos\delta = 0.936$ mas yr^{-1}, $\mu_\delta = -1.23$ mas yr^{-1}; ref. [37]). Specifically, we selected stars with proper motions and proper motion uncertainties that are consistent within 2σ of the following bounds:

0.4 mas yr$^{-1} < \mu_\alpha \cos\delta < 1.2$ mas yr^{-1},
−1.4 mas yr$^{-1} < \mu_\delta < -1.0$ mas yr^{-1} (Extended Data Fig. 1).

These proper motion ranges were chosen to roughly correspond to the proper motions of stars that were previously confirmed to be members of Tucana II[15,17]. Note that we slightly relaxed this proper motion criterion for one candidate member—it was subsequently found to be a non-member. We then selected a sample of 22 metal-poor red giant stars with proper motions similar to that of Tucana II to observe with the MagE spectrograph. Observing priority was given to stars with photometric $[Fe/H] < -1.5$, as more metal-poor stars have increased likelihood of being members. Full observational details are given in Supplementary Table 1, and the SkyMapper colour–colour plots from which stars were identified as metal-poor giants are shown in Extended Data Fig. 2.

Before the Gaia DR2 data release or any of our Tucana II SkyMapper photometry studies, we had already taken spectra of 43 stars with the IMACS spectrograph[24] (more details given below). This early target selection was solely based on choosing stars with $g - r$ colours within 0.1 mag of a 12 Gyr, $[Fe/H] = -2.5$ isochrone[38] overlaid at the distance modulus of Tucana II[18,19] on a g, r colour–magnitude diagram of stars within 20′ of the centre of the system, along with a few horizontal branch candidates. This colour–magnitude diagram had been generated by running the SExtractor software[39] with default parameters on Dark Energy Survey (DES) images of Tucana II obtained from the National Optical Astronomy Observatory public data archive[40,41].
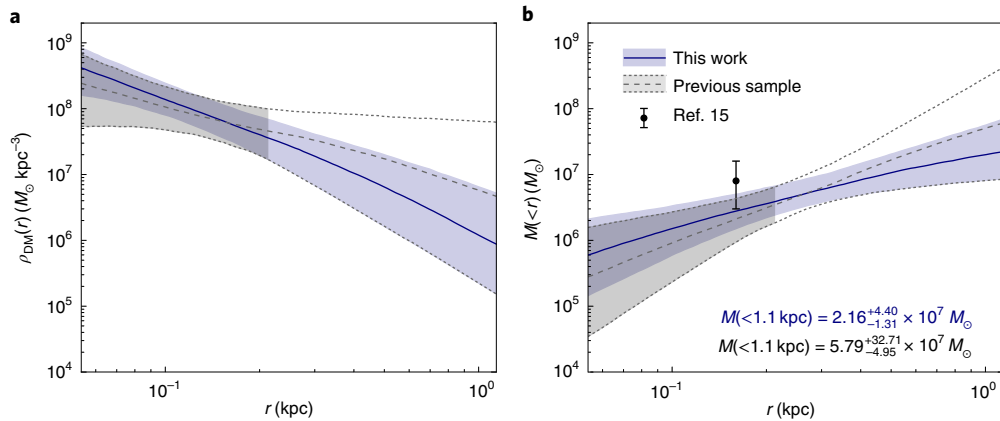
Fig. 2 | Mass modelling of Tucana II out to 1 kpc. a, Density profiles $\rho_{DM}(r)$ of Tucana II, derived using data from previous spectroscopic work[15] shown in grey (dashed and dotted lines) and from including the new stars in blue (solid line). The error bounds correspond to 1σ uncertainties from the posterior density distribution. **b**, Enclosed mass $M(<r)$ as a function of distance r, derived using data from previous spectroscopic studies[15] shown in grey (dashed and dotted lines) and from including the new members in blue (solid line). An enclosed mass measurement within a half-light radius[18] using the velocity dispersion and 1σ uncertainty from ref. [15] is shown as the black data point. The error bounds correspond to 1σ uncertainties from the posterior mass distribution in our modelling.

Spectroscopic observations. We obtained spectra of 22 candidate members of the Tucana II ultrafaint dwarf galaxy using the MagE spectrograph[23] on the Magellan Baade telescope on 3–5 August 2019. Data were obtained using 1×1 on-chip binning and a 0.7″ slit, which granted a resolving power of ~6,000, and spanning a wavelength range of ~320 nm to ~1,000 nm. The seeing was excellent (<0.6″) for the duration of these observations. The MagE data were reduced using the CarPy reduction pipeline[42]. From a subsequent radial velocity analysis of these spectra (Radial velocity analysis), ten of these 22 candidates were confirmed as members of Tucana II. A thorium–argon lamp frame was obtained for wavelength calibration after slewing to each target. Our targets had g magnitudes between 17.5 and 20.5, and each star was observed for at least 10 min. For the purposes of more accurate metallicity determinations, the two most metal-poor stars in our sample were observed for more extended periods of time.

A full summary of our MagE observations, including total exposure times and signal-to-noise values, is provided in Supplementary Table 1. Examples of our MagE spectra are shown in Extended Data Fig. 3.

We had also obtained spectra of 43 stars in the field of the Tucana II ultrafaint dwarf galaxy using the IMACS spectrograph[24] on 23–25 July 2015, 25 May 2016 and 5–7 August 2016. These spectra were obtained simultaneously by using the multislit mode of the spectrograph with the f/4 camera, which granted a $15.4' \times 15.4'$ field of view. A slit size of 0.7″ and a 1,200 lines mm^{-1} grating were used for these observations, which resulted in a resolving power of ~11,000 and a dispersion of 0.19 Å per pixel over the wavelength range of these spectra (~750 nm to ~900 nm). We note that this spectral range was chosen to cover the prominent telluric absorption feature at ~760 nm and the calcium triplet lines at 849.8 nm, 854.2 nm and 866.2 nm. Due to the configuration of the multislit mask used for these observations, the actual wavelength range varied from star to star, but slits were placed such that, at minimum, the calcium triplet region was included. Our observing strategy followed that of previous IMACS spectroscopic studies of ultrafaint dwarf galaxy stars[43,44], except that we used a HeNeAr comparison lamp in each of our observations. A total of $14 \times 2,700$ s exposures were taken in July 2015 in mediocre seeing conditions (~1.0″ seeing), $4 \times 2,700$ s exposures in May 2016 in poor seeing conditions (>1.0″) and $8 \times 2,700$ s in generally fair seeing conditions (~0.9″) in August 2016. We reduced our data in the exact manner as outlined in the aforementioned studies, utilizing the COSMOS pipeline[45,46] and a modified version of the DEEP2 reduction pipeline[47,48].

Radial velocity analysis. We derived radial velocities closely following methods of refs. [43,44] when analysing our IMACS spectra, and with slight modifications when analysing our MagE spectra to account for instrumental differences, differences in wavelength range and resolution. We briefly describe both analyses here.

The velocities from the IMACS spectra were derived by chi-squared fits[49] to a template IMACS spectrum of the bright, metal-poor giant HD 122563[50] observed in the same configuration as the multislit observations. The chi-squared fits were performed over the wavelength range from 845 nm to 868 nm, and a velocity of -26.51 km s^{-1} was assumed for HD 122563[51]. Velocity corrections for the miscentring of stars in their slits were computed by performing this same procedure over the telluric A-band region (750 nm to 770 nm) using a spectrum of the rapidly rotating hot star HR 4781[43]. These velocity corrections from the A-band region showed a systematic dependence on the position of the slit on the

chip[43,44]. Therefore, we fitted a linear relation between the velocity correction and the slit position and applied the velocity correction from the A band following this relation. This had the advantage of being applicable to spectra with A-band regions not covered in the spectral range or with low S/N. Heliocentric corrections were computed using the Astropy package[52,53].

The velocities from the MagE spectra were derived by cross-correlating the observed spectra with a template MagE spectrum of HD 122563 observed in the same configuration. The cross-correlation was performed over a wavelength region encompassing the prominent magnesium b absorption feature (490 nm to 540 nm), and the velocity of HD 122563 was again assumed to be -26.51 km s^{-1}. The A-band region of an IMACS spectrum of HR 4781[43] that was smoothed to the resolution of the MagE spectra (resolution $\approx 6,700$) was used to perform any corrections for the miscentring of the stars in the slit.

The uncertainties on our velocity measurements were derived by adding in quadrature the statistical uncertainty with an estimate of the systematic uncertainty, following previous work[43,44,49]. To derive the statistical uncertainty, we first re-added random noise to each spectrum on the basis of its noise level as estimated from its signal-to-noise ratio, remeasured the velocity, and then repeated this procedure 500 times[49]. Then, the statistical uncertainty was defined as the s.d. of the resulting distribution of velocities, after removing 5σ outliers. To derive the systematic uncertainty, we computed velocities and statistical uncertainties for spectra that were obtained from individual exposures. We then derived the systematic uncertainty as the additional uncertainty needed to account for the variation in velocities across exposures for each star. The systematic uncertainty for the IMACS spectra was determined to be 1.2 km s^{-1}, which agrees with previous work[43,44]. The systematic uncertainty for the MagE data was determined to be 2.95 km s^{-1}, probably due to the lower resolution (resolution $\approx 6,700$) relative to the IMACS data (resolution $\approx 11,000$).

Final velocities from the IMACS spectra were taken as the weighted average of velocity measurements from stacked spectra from each observing run, where each measurement was weighted by the inverse square of the uncertainty. We excluded likely binaries, which were identified as stars with at least one 2σ discrepancy in their radial velocities across epochs, from this step. Final velocities for the MagE spectra were calculated in the same way, except that a weighted average was taken over velocity measurements from stacked spectra for each night of observation. All velocity measurements and uncertainties are listed in Supplementary Table 2.

We derive a systemic velocity for Tucana II of -126.3 ± 1.5 km s^{-1} and a velocity dispersion of $4.6^{+1.5}_{-1.1}$ km s^{-1} using our sample of MagE and IMACS members. We implemented a maximum likelihood estimate following ref. [54] using the emcee Python package[55] to derive these values. Our systemic velocity and velocity dispersion are consistent with previous measurements of those quantities for Tucana II[15], but have notably smaller uncertainties. Our measurements imply that Tucana II has a mass of $(2.4^{+1.9}_{-1.2}) \times 10^6 M_\odot$ within a half-light radius, following ref. [56]. We note that performing this analysis for a subsample of only the MagE spectra and another subsample of only the IMACS spectra returns Tucana II systemic velocities separated by ~1.3 km s^{-1}, which is well within the statistical uncertainty in the systemic velocity. This suggests no notable systematic offset in the velocities derived from each instrument. Excluding the Tucana II star most likely to be a non-member (Tuc2-309; Membership confirmation) lowers our velocity dispersion by only ~5%.

Metallicity analysis. From the MagE spectra, we derived metallicities using the magnesium b absorption feature (~515 nm) and the calcium triplet lines (849.8 nm, 854.2 nm and 866.2 nm). From the IMACS spectra, we solely used the calcium triplet lines. We used an empirical calibration to derive metallicities from the calcium triplet lines[57], and employed standard spectral synthesis techniques to derive metallicities from the magnesium b region. Our particular implementation of these techniques is comprehensively described in previous work with MagE spectra of dwarf galaxy stars[58], which we summarize here.

Stellar metallicities can be derived from the equivalent widths of the calcium triplet lines in combination with the absolute V magnitude of the star[57]. For our MagE spectra, we measured the equivalent widths of the calcium triplet lines by fitting the Voigt1D model in the astropy.modeling package to each line. The spectra were continuum normalized by iteratively fitting a third-order spline after masking absorption features. For fits requiring additional attention due to, for example, poor estimates of the stellar continuum, equivalent widths were measured using the splot task in IRAF[59,60]. The absolute V magnitude was derived for each star using colour transformations from the DES photometric system[18] and the distance modulus of Tucana II[18,19]. Random uncertainties were derived by remeasuring the equivalent widths after varying the continuum level by 1σ according to the S/N of each spectrum, and adopting a systematic uncertainty of 0.17 dex (ref. [57]) for the calcium triplet metallicity calibration. For our IMACS spectra, we fitted the calcium triplet lines and derived uncertainties following previous studies of dwarf galaxies with IMACS[44]. We find that our IMACS metallicities agree within 1σ with literature metallicities for the two stars that have metallicities from previous spectroscopic work of Tucana II[17].

We measured metallicities from the magnesium b region by fitting synthetic spectra of varying abundances to the observed spectrum. The syntheses and fitting were performed with the Spectroscopy Made Hard software[61] using a 2017 version of the MOOG radiative transfer code[62] that has an updated treatment of scattering[63] and the ATLAS9 model atmospheres[64]. The line list was compiled from various sources[65–68] using software provided by C. Sneden (personal communication). The effective temperature and surface gravity of each star are required as inputs for the spectral synthesis. Initial stellar parameters were derived by matching the $g-r$ colours of the Tucana II stars[69] to those on an [Fe/H] = −2.5, 12 Gyr isochrone[38].

To test this method we also derived stellar parameters in this manner for stars with known stellar parameters[17]. We find on average higher effective temperatures by 120 K and higher $\log g$ by 0.33 dex compared with the literature results. We therefore correct our stellar parameter measurements by these values in our analysis. We obtain random uncertainties by noting the variation in [Fe/H] required to encompass most of the noise in the absorption feature. Systematic uncertainties were derived by remeasuring [Fe/H] after varying the effective temperature by 150 K and the surface gravity by 0.3 dex. We note that all of our Tucana II members that were observed with MagE have metallicity measurements dominated by the systematic uncertainty, due to the relatively high signal-to-noise ratio (>25) of their spectra. Using these methods, we derive metallicities that agree with literature values for the standard stars CD 38-245 ([Fe/H] = −3.97; literature [Fe/H] = −4.06; ref. [70]), CS 22897-052 ([Fe/H] = −3.11; literature [Fe/H] = −3.08; ref. [70]) and HD 122563 ([Fe/H] = −2.57; literature [Fe/H] = −2.64; ref. [50]) that were also observed by the MagE spectrograph.

We find that our metallicities from the magnesium b synthesis generally agree well with metallicities from the calcium triplet method. The metallicity differences have a mean value of 0.01 dex and an s.d. of 0.26 dex, suggesting no systematic offset. We note that one distant star (Tuc2-309) has notably different calcium triplet ([Fe/H] = −1.77) and magnesium b ([Fe/H] = −2.47) metallicities. Upon inspection of its spectrum, this star appears to be genuinely deficient in magnesium, or unusually enhanced in calcium, rendering its overall metallicity somewhat ambiguous. For consistency with our other measurements, we still report its metallicity as the weighted average of the calcium triplet and magnesium b metallicities. Further investigation of systematic offsets from the few stars in common between our MagE, IMACS and MIKE datasets shows that they have metallicities consistent within uncertainties. The stars in common between the samples are indicated in Supplementary Table 2.

The final metallicity measurements were derived by taking the weighted average of the metallicities from the calcium triplet lines and the magnesium b region (for the MagE spectra), or simply from the calcium triplet lines (for the IMACS spectra). Due to reduction issues (for example, bad sky subtraction), we estimate the equivalent width of the reddest calcium triplet line for two stars (Tuc2-303 and Tuc2-319) by taking it to be 0.62 times the sum of the equivalent widths of the other two calcium triplet lines. The value of 0.62 is the mean of the corresponding ratio of equivalent widths for the other Tucana II members. As an additional quality criterion, we only report metallicities from IMACS spectra with S/N greater than or equal to 10. All the metallicities and uncertainties of Tucana II members are presented in Supplementary Table 3.

The mean metallicity of Tucana II was calculated as the average of the metallicities of its member stars, weighted by the squared inverse of their metallicity uncertainty. If available, metallicities from high-resolution MIKE spectra were assumed as the stellar metallicities. Otherwise, metallicities from medium-resolution MagE and IMACS spectra were used. We used metallicities from M2FS spectra[15] for the two stars in that study listed as likely members

(membership probability > 0.90) but not later reobserved. We reduced these M2FS metallicities by 0.32 dex, which is necessary to undo an artificial offset and bring the metallicities of the entire M2FS sample into agreement with those from high-resolution spectra[17].

We find evidence that the most distant stars in Tucana II tend to be more metal poor than the central population (Fig. 1b). At face value, the weighted average of the metallicities of stars within two half-light radii[18] (⟨[Fe/H]⟩ = −2.62 ± 0.05) is notably higher than the metallicities of stars outside two half-light radii (⟨[Fe/H]⟩ = −3.02 ± 0.07). To test the robustness of this difference, we first constructed a Gaussian Metallicity Distribution Function (MDF) of the inner region in which the mean and σ of the metallicities of the inner stars set the mean and σ parameters of the Gaussian. We then drew seven members from this MDF for 10^4 instances and calculated the sample's mean metallicity in each instance. We find that the resulting distribution of these mean metallicities is centred on [Fe/H] = −2.66 and has an s.d. of 0.11 dex, still returning a statistically significant difference from the mean metallicity of the outer stars. Consequently, the differential in metallicities between the inner and outer stars is robust.

To test whether a linear model could describe the dependence of the metallicities on spatial distance, we performed a linear fit to the stellar metallicities as a function of their distance from the centre of Tucana II. This returned a statistically significant slope of −0.87 ± 0.30 dex kpc⁻¹. We note that this result rests on the existence of the farthest star in Tucana II; however, given its low metallicity of [Fe/H] = −3.50 there is little doubt that this star is not a member. For reference, if we were to exclude it, the resulting slope of −0.75 ± 0.68 dex kpc⁻¹ would no longer be statistically significant. However, excluding the distant star that has the highest probability of being a foreground star, Tuc2-309 (see 'Membership confirmation'), results again in a more statistically significant slope of −0.99 ± 0.25 dex kpc⁻¹. This highlights the need for a larger sample of distant members to further validate the existence of any such gradient.

As an additional consideration, we also implemented a maximum-likelihood approach following ref. [71], in which the likelihood function contains a linear metallicity gradient term in addition to a metallicity dispersion term and a mean metallicity term. We implemented this likelihood estimator using the emcee Python package[55]. This analysis returns a slope of 0.69 ± 0.38 dex kpc⁻¹, which suggests a linear gradient, but is still inconclusive. At face value, our derived metallicity gradient for Tucana II is −0.08 dex r_h^{-1}, assuming the Tucana II half-light radius in ref. [18]. This is comparable to other metallicity gradients seen in larger dwarf spheroidal galaxies[72].

Membership confirmation. Members of ultrafaint dwarf galaxies are generally identified through a joint analysis of their metallicities and radial velocities, since ultrafaint dwarf galaxy stars tend to be far more metal poor than foreground Milky Way stars and have clustered radial velocities. We identified members as stars with radial velocities within three times the velocity dispersion of Tucana II around the mean radial velocity of Tucana II (−141 km s⁻¹ to −110 km s⁻¹) and with metallicities [Fe/H] ≲ −2.0. It is unlikely that we excluded members on the basis of the velocity threshold—no stars had radial velocities just beyond these cutoffs. However, one distant star (Tuc2-309) has a metallicity just above this threshold ([Fe/H] = −1.95), but a radial velocity and proper motion still consistent with membership. We therefore regard it as a likely member. Both the mean metallicity (~−2.8) and systemic radial velocity (~−126 km s⁻¹) of Tucana II are well separated from the corresponding values of the foreground stellar population, granting confidence to this particular scheme of confirming membership status. However, given the distant nature of our newly identified members, we performed an additional check on their membership likelihood.

In Extended Data Fig. 4, we show the predicted halo distribution of radial velocities and metallicities for stars in the vicinity of Tucana II from the Besancon stellar population model[73], after replicating our isochrone, [Fe/H], and $\log g$ target selection cuts. We find that 0.4% of these stars satisfy our velocity and metallicity criteria for Tucana II membership. By replicating our isochrone, [Fe/H], and $\log g$ cuts but relaxing the proper motion cut on our SkyMapper catalogue, we estimate that there are 260 foreground metal-poor giant stars within about nine half-light radii of Tucana II. If 0.4% of these stars satisfy our membership criteria, this would result in about one false positive in our sample of Tucana II members. However, we note that the false positive rate drops off rapidly at lower metallicities. Restricting the range of membership metallicities to [Fe/H] < −2.5 results in a rate of 0%. Thus, while one of our more metal-rich Tucana II members could conceivably be a foreground star, there is a negligible chance that the farthest member is falsely classified, given its very low metallicity of [Fe/H] = −3.50. It is also extremely unlikely that any members beyond two half-light radii are falsely classified, given that their metallicities are all below [Fe/H] = −2.5, except for Tuc2-309.

In Supplementary Table 2, we list the membership status of every star in our sample. We identify stars that meet the above radial velocity and metallicity criteria as members. Some stars in our sample have radial velocity measurements that satisfy the velocity criterion, but do not have metallicities as their spectra have $S/N < 10$. We identify these stars as likely members. We note that all members have proper motions consistent with the bounds defining the Tucana II stellar membership as listed in Selection of candidate members.

In total, we count 19 members of Tucana II: eight stars that were listed in the M2FS sample as having membership probability of >0.9 (ref. [15]), two additional members identified with the MIKE spectrograph[17], one additional member identified in our IMACS sample and eight additional members identified in our MagE sample. In total, seven members were observed with the MIKE spectrograph[17], five members were observed with IMACS and ten members were observed with MagE. There were an additional three stars in the IMACS dataset (two of which were also observed with M2FS) with velocities consistent with membership of Tucana II, but no metallicity value due to low S/N. Full details are presented in Supplementary Table 2.

Comparison with canonical stellar density profiles. We tested whether the spatial distribution of Tucana II member stars is compatible with either an exponential or a Plummer stellar density profile. Specifically, we drew samples of 19 members 10,000 times from each distribution to test the likelihood of observing 12 stars within two half-light radii and seven stars beyond that distance. We find that this happens in 7% of cases under a Plummer profile and in 2% of cases under an exponential profile. Excluding our distant member that is most likely to be a foreground star, Tuc2-309, leads to 15% of cases under a Plummer profile fulfilling our criterion. However, we caution that these numbers are very sensitive to the choice of structural parameters for Tucana II.

We assume a half-light radius of 7.2′ for Tucana II[18] in this analysis. We opt for this value over other studies[19,74] after performing several tests. First, we compared the half-light radii reported in each study with those determined from deeper follow-up photometry for seven systems[75–80]. These seven systems were chosen as they were the only systems in ref. [18] that have published deeper photometric studies. We find that the half-light radii reported in ref. [8] agree within 2σ of all of the deeper studies. Additionally, we calculated residuals by subtracting the reported half-light radii in refs. [18,19,74] from the half-light radii determined from the deeper imaging studies. We find that ref. [18] has residuals with a marginally lower standard deviation (~0.5′) when compared with residuals from other work (~1.0′). Moreover, we note that the reported position angle and ellipticity for Tucana II in refs. [19,74] would be discrepant with the location of our most distant Tucana II members. For these reasons, we assume the structural parameters from ref. [18].

For completeness, we note that, if we were to assume the elliptical half-light radii in refs. [19,74], the distances of the farthest two stars would be 5.1 and 8.1 elliptical half-light radii, and 4.5 and 6.6 half-light radii, respectively. These radii would lead to more agreement with a Plummer profile. As a consequence, we cannot claim a discrepancy with these canonical profiles until deeper photometry of Tucana II is obtained.

From Extended Data Fig. 1 of candidate members, spectroscopic observations of stars can be regarded as complete down to $g \approx 19.5$ within the inner region of the galaxy, but probably incomplete in the outer regions (beyond three half-light radii). This implies that additional distant members of the galaxy may be discovered in the future. If more stars were known in the extended halo, the underlying stellar density distribution would stray even further from any canonical density profile.

Finally, we note that there are multiple distance measurements of Tucana II in the literature, with all measurements being consistent within 2 kpc (refs. [18,19,81]). For consistency with our choice of structural parameters, we adopt a distance of 58 kpc from ref. [18] throughout our analysis.

Systemic proper motion of Tucana II. We derive the systemic proper motion of Tucana II by taking the weighted average of the Gaia DR2 proper motions[22,36] of members brighter than $g = 20$ in Supplementary Table 2. Each weight was taken as the inverse square of the measurement uncertainty. We derive a systemic $\mu_\alpha \cos \delta = 0.955 \pm 0.047$ mas yr^{-1} and a systemic $\mu_\delta = -1.212 \pm 0.058$ mas yr^{-1}.

Modelling of tidal disruption. To determine the expected location of tidal debris from Tucana II, we simulate its tidal disruption and subsequent stream formation using the modified Lagrange Cloud stripping technique[82], which has been updated to include the influence of the Large Magellanic Cloud (LMC)[83]. Including the LMC is crucial since it can deflect tidal debris, leading to a notable misalignment between the progenitor's orbit and tidal debris[83,84]. We use a realistic Milky Way model[85] and the machinery of GalPot[86] to evaluate accelerations in this potential. Motivated by recent fits to the LMC mass[83], we treat the LMC as a Hernquist profile[87] with a mass of $1.5 \times 10^{11} M_\odot$ and a scale radius of 17.13 kpc. We integrate Tucana II backwards for 5 Gyr starting from its present distance[19], proper motions[88] and radial velocity from this work. The LMC is similarly integrated backwards starting with its present-day observables[89–91]. We model the progenitor of Tucana II as a Plummer sphere with a conservative mass estimate of $2 \times 10^6 M_\odot$ (ref. [15]) and a scale radius of 100 pc. This produces tidal debris that is well aligned with the orbit. This shows that the debris should be aligned with the track shown in Fig. 1 with a small offset of $-2 \pm 4°$ on the sky. We find that this alignment is not sensitive to the precise choice of the total mass of Tucana II.

We derived the tidal radius of Tucana II using the galpy[92] Python library. Specifically, we instantiated an orbit using the orbital parameters of Tucana II[37] and derived a tidal radius using the rtide function[93] under the Milky Way potential MWPotential14. We then derived tidal radii for various masses of Tucana II to determine at what mass the tidal radius encompasses the distance to the farthest

member (1.11 kpc). This occurred for a mass of $1.3 \times 10^7 M_\odot$, which we take as the lower limit on the Tucana II mass. We note that our choice of MWPotential14 is consistent with reporting a lower bound on the Tucana II mass. MWPotential14 is a low estimate for the Milky Way mass, and adopting a higher Milky Way mass would only increase the Tucana II mass required to bound its farthest member.

We also tested whether the spatially extended members of Tucana II display a velocity gradient, which is a signature of tidally disrupting systems[26]. To do this, we searched for a velocity gradient by implementing the velocity-relevant terms of the likelihood estimator in ref. [71]. This likelihood estimator includes a term for the slope of a velocity gradient and a term for the position angle corresponding to the axis of the gradient, in addition to typical terms corresponding to the velocity dispersion and mean velocity. We implemented this likelihood estimator using the emcee Python package[55] and performed this analysis on the 17 Tucana II members from the M2FS, IMACS and MagE samples. The analysis returned no detected velocity gradient $0.13^{+0.17}_{-0.14}$ km s^{-1}′$^{-1}$. Our 2σ upper limit on the velocity gradient would therefore be 0.45 km s^{-1}′$^{-1}$. The 2σ upper limit is 0.43 km s^{-1}′$^{-1}$ if Tuc2-309, the distant star most likely to be a non-member, is excluded. We note that fixing the axis of the gradient to span the direction of our most distant star results in a slope of 0.0 ± 0.07 km s^{-1}′$^{-1}$.

Modelling of dark matter density profile. We model the density profile of the dark matter halo of Tucana II using a Jeans modelling procedure[94–96]. For completeness, we briefly outline the most important steps here but more details are reported in ref. [97].

The three-dimensional distribution of the stars is modelled by a Plummer profile,

$$\nu(r) = \frac{3L}{4\pi a^3} \left(1 + \frac{r^2}{a^2}\right)^{-\frac{5}{2}}$$

where L is the total luminosity and a is the scale length of the distribution. Given that the system is observed in projection, we use the surface brightness profile

$$I(R) = \frac{L}{\pi a^2} \left(1 + \frac{R^2}{a^2}\right)^{-2}$$

where R is the projected radius, while r is the three-dimensional radius from the centre of the dwarf. Because the stars contribute negligibly to the gravitational potential, the value of L does not carry physical influence.

We model the density profile of dark matter by a generalized NFW profile[98],

$$\rho_{DM}(r) = \rho_0 \left(\frac{r}{r_s}\right)^{-\gamma} \left(1 + \frac{r}{r_s}\right)^{-(3-\gamma)}$$

where the free parameters that we fit for are the overall density normalization (ρ_0), the scale radius (r_s) and the slope of the inner profile (γ). We assume that the system is spherical and in equilibrium, and solve the projected Jeans equation

$$\sigma_p^2(R)I(R) = 2 \int_R^\infty \left(1 - \beta(r)\frac{R^2}{r^2}\right) \left(\frac{\nu(r)\sigma_r^2(r)r}{\sqrt{r^2 - R^2}}\right) dr$$

where σ_p is the projected velocity dispersion along the line of sight, σ_r is the radial velocity dispersion in three dimensions and $\beta(r) = 1 - (\sigma_\theta^2 + \sigma_\phi^2)/(2\sigma_r^2)$ is the velocity anisotropy of the stars. The variables σ_r, σ_ϕ and σ_θ are the velocity dispersions in spherical coordinates. The radial velocity dispersion is the solution to

$$\frac{1}{\nu} \left[\frac{\partial}{\partial r}(\nu \sigma_r^2) + \frac{2\beta(r)}{r}(\nu \sigma_r^2)\right] = -\frac{GM(<r)}{r^2}$$

where G is the gravitational constant, and $M(<r)$ is calculated from the density profile of dark matter.

We use an unbinned likelihood function[99] to take into account the individual velocity uncertainties of each star, first assuming that the system is isotropic ($\beta(r) = 0$). The likelihood is defined as

$$\mathcal{L} = \prod_{i=1}^{N_{stars}} \frac{(2\pi)^{-1/2}}{\sqrt{\sigma_p^2(R_i) + \Delta_{v_i}^2}} \exp\left[-\frac{1}{2}\left(\frac{(v_i - \bar{v})^2}{\sigma_p^2(R_i) + \Delta_{v_i}^2}\right)\right]$$

We use a Markov chain Monte Carlo procedure to find the best fit parameters, assuming uniform priors on $\log_{10}[\rho_0 (M_\odot \text{ kpc}^{-3})]$ of [2.2, 13.0], $\log_{10}[r_s(\text{kpc}^{-1})]$ of [−3.0, 2.0], γ of [−1, 3] and average velocity $\bar{v}$ (km s^{-1}) of [−200, 200]. We fix $a = 120$ pc following the reported half-light radius in ref. [18]. Varying a by ± 30 pc (the uncertainty in the half-light radius in ref. [18]) changes our final density and mass profiles at the ~5% level—far below our 1σ uncertainties on these quantities.

Given the large swaths of literature on the mass anisotropy degeneracy (see ref. [93] and references therein), we also rerun the mass modelling assuming the standard Osipkov–Merritt anisotropy[100,101], defined as

$$\beta(r) = \frac{r^2}{(r^2 + r_a^2)}$$

where r_a is the anisotropy parameter for which we fit, which describes the transition of the anisotropy from $\beta = 0$ at small radii to $\beta = 1$ at large radii. We assume a prior on $\ln[r_a \, (\text{kpc})]$ of $[-5, 0]$ to ensure that the transition radius occurs before the location of the farthest star. We find that the mass of the system with this anisotropy model increases to $(4.6^{+7.7}_{-3.1}) \times 10^7 \, M_\odot$ within 1 kpc, which is within a 1σ variation of the mass in the isotropic case of $(2.2^{+4.4}_{-1.3}) \times 10^7 \, M_\odot$. Furthermore, adopting the most extreme cases of constant velocity anisotropy still only varies our results at the $\sim 1\sigma$ level relative to the mass derived assuming isotropy. Assuming constant radial anisotropy ($\beta = 1$) increases our mass estimate to $(7.8^{+9.3}_{-4.7}) \times 10^7 \, M_\odot$, while assuming extreme constant tangential anisotropy ($\beta = -9$) still results in a large mass of $(0.9^{+1.5}_{-0.5}) \times 10^7 \, M_\odot$ within 1 kpc.

As presented in Fig. 2, we performed the above analysis on two samples to investigate the effect of adding our newly discovered members using IMACS and MagE to the body of known members in the literature. The first sample is simply the previously known red giant members in the literature with precise velocity measurements[15]. The second sample is composed of previously known members and our newly discovered members. We note that the sample of eight red giant members in ref. [15] has a systemic velocity ($\sim -127.3 \, \text{km s}^{-1}$) similar to the systemic velocity of just our newly discovered members ($\sim -126.3 \, \text{km s}^{-1}$), suggesting no statistically meaningful velocity systematics across the two samples. We note that our new addition of distant members meaningfully affects the mass measurement out to large distances. As seen in Fig. 2, the uncertainty on the inferred enclosed mass drops by a factor of at least ~ 3 from our additional members. Since this is a much larger drop than would be expected from doubling the sample of members, it is likely that the extended spatial distribution of new members meaningfully affects the mass determination.

We note that the theoretically derived mass estimate from this method, and any larger mass estimates, are supported by our observationally derived lower bound of $1.3 \times 10^7 \, M_\odot$ that is required to ensure that the most distant Tucana II member is gravitationally bound to the system.

We also derive the enclosed mass within 1 kpc of a $10^8 \, M_\odot$ NFW halo to compare our results with recent bounds on the minimum halo mass[28]. We begin this calculation by using the Python package Halotools v0.7[102] to initialize a $10^8 \, M_\odot$ halo with a concentration parameter of 26 (ref. [103]). We then use the enclosed_mass method to calculate that a mass of $2.5 \times 10^7 \, M_\odot$ exists within 1 kpc of such an NFW halo, which is comparable to the mass we derive within 1 kpc of Tucana II.

Data availability
The velocity and metallicity measurements that support the findings of this study are presented in Supplementary Tables 1, 2 and 3. The individual stellar spectra from which these measurements were derived and any supplementary material (for example line lists) are available from the corresponding author upon reasonable request. The proper motions of the stars analysed in this paper are publicly available from the Gaia DR2 archive (http://gea.esac.esa.int/archive/). Source data are provided with this paper.

Code availability
The stellar synthesis code MOOG can be retrieved from https://github.com/alexji/moog17scat. The other codes used in this analysis are the authors' implementations of published techniques (for example, calcium ɪɪ K and calcium triplet calibrations), and are available from the corresponding author upon reasonable request.

References
1. Willman, B. et al. A new dwarf galaxy in Ursa Major. *Astrophys. J.* **626**, L85–L88 (2005).
2. Belokurov, V. Galactic archaeology: the dwarfs that survived and perished. *New Astron. Rev.* **57**, 100–121 (2013).
3. Simon, J. D. The faintest dwarf galaxies. *Annu. Rev. Astron. Astrophys.* **57**, 375–415 (2019).
4. Bromm, V. & Yoshida, N. The first galaxies. *Annu. Rev. Astron. Astrophys.* **49**, 373–407 (2011).
5. Brown, T. M. et al. Quenching of the ultra-faint dwarf galaxies in the reionization era. *Astrophys. J.* **796**, 91–103 (2014).
6. Kirby, E. N. et al. The universal stellar mass–stellar metallicity relation for dwarf galaxies. *Astrophys. J.* **779**, 102–122 (2013).
7. Frebel, A., Simon, J. D. & Kirby, E. N. Segue 1: an unevolved fossil galaxy from the early universe. *Astrophys. J.* **786**, 74–82 (2014).
8. Deason, A., Wetzel, A. & Garrison-Kimmel, S. Satellite dwarf galaxies in a hierarchical universe: the prevalence of dwarf–dwarf major mergers. *Astrophys. J.* **794**, 115–122 (2014).
9. Munshi, F. et al. Dancing in the dark: uncertainty in ultrafaint dwarf galaxy predictions from cosmological simulations. *Astrophys. J.* **874**, 40–52 (2019).
10. Wheeler, C. et al. Be it therefore resolved: cosmological simulations of dwarf galaxies with 30 solar mass resolution. *Mon. Not. R. Astron. Soc.* **490**, 4447–4463 (2019).
11. Rey, M. P. et al. EDGE: the origin of scatter in ultra-faint dwarf stellar masses and surface brightnesses. *Astrophys. J. Lett.* **886**, L3–L7 (2019).
12. Munoz, R. R. et al. A MegaCam survey of outer halo satellites. III. Photometric and structural parameters. *Astrophys. J.* **860**, 66–109 (2018).
13. Frebel, A., Norris, J. E., Gilmore, G. & Wyse, R. F. G. The chemical evolution of the Bootes I ultra-faint dwarf galaxy. *Astrophys. J.* **826**, 110–123 (2016).
14. Norris, J. E., Gilmore, G., Wyse, R. F. G., Yong, D. & Frebel, A. An extremely carbon-rich, extremely metal-poor star in the Segue 1 system. *Astrophys. J. Lett.* **722**, L104–L109 (2010).
15. Walker, M. G. et al. Magellan/M2FS spectroscopy of Tucana 2 and Grus 1. *Astrophys. J.* **819**, 53–63 (2016).
16. Ji, A. P., Frebel, A., Ezzeddine, R. & Casey, A. R. Chemical diversity in the ultra-faint dwarf galaxy Tucana II. *Astrophys. J. Lett.* **832**, L3–L9 (2016).
17. Chiti, A. et al. Chemical abundances of new member stars in the Tucana II dwarf galaxy. *Astrophys. J.* **857**, 74–86 (2018).
18. Bechtol, K. et al. Eight new Milky Way companions discovered in first-year Dark Energy Survey data. *Astrophys. J.* **807**, 50–65 (2015).
19. Koposov, S., Belokurov, V., Torrealba, G. & Evans, N. W. Beasts of the southern wild: discovery of nine ultra faint satellites in the vicinity of the Magellanic Clouds. *Astrophys. J.* **805**, 130–147 (2015).
20. Keller, S. C. et al. The SkyMapper telescope and the Southern Sky Survey. *Publ. Astron. Soc. Aust.* **24**, 1–12 (2007).
21. Chiti, A., Frebel, A., Jerjen, H., Kim, D. & Norris, J. E. Stellar metallicities from SkyMapper photometry I: a study of the Tucana II ultra-faint dwarf galaxy. *Astrophys. J.* **891**, 8–31 (2020).
22. The Gaia Collaboration. Gaia Data Release 2. *Astron. Astrophys.* **616**, E1 (2018).
23. Marshall, J. L. et al. The MagE spectrograph. *Proc. SPIE* **714**, 54–63 (2008).
24. Dressler, A., Hare, T., Bigelow, B. C. & Osip, D. J. IMACS: the wide-field imaging spectrograph on Magellan-Baade. *Proc. SPIE* **6269**, 62690F (2006).
25. Tolstoy, E. et al. Two distinct ancient components in the Sculptor dwarf spheroidal galaxy: first results from the dwarf abundances and radial velocities team. *Astrophys. J.* **617**, L119–L122 (2004).
26. Li, T. S. et al. The first tidally disrupted ultra-faint dwarf galaxy?: A spectroscopic analysis of the Tucana III stream. *Astrophys. J.* **866**, 22–44 (2018).
27. Read, J. I. & Erkal, D. Abundance matching with the mean star formation rate: there is no missing satellites problem in the Milky Way above $M_{200} \sim 10^9 \, M_\odot$. *Mon. Not. R. Astron. Soc.* **487**, 5799–5812 (2019).
28. Jethwa, P., Erkal, D. & Belokurov, V. The upper bound on the lowest mass halo. *Mon. Not. R. Astron. Soc.* **473**, 2060–2083 (2018).
29. Agertz, O. et al. EDGE: the mass–metallicity relation as a critical test of galaxy formation physics. *Mon. Not. R. Astron. Soc.* **491**, 1656–1672 (2020).
30. Magg, M. et al. Predicting the locations of possible long-lived low-mass first stars: importance of satellite dwarf galaxies. *Mon. Not. R. Astron. Soc.* **473**, 5308–5323 (2018).
31. Bessell, M. et al. SkyMapper filter set: design and fabrication of large-scale optical fibers. *Publ. Astron. Soc. Pac.* **123**, 789–797 (2011).
32. Da Costa, G. S. et al. The SkyMapper DR1.1 search for extremely metal-poor stars. *Mon. Not. R. Astron. Soc.* **489**, 5900–5918 (2019).
33. Murphy, S. et al. SkyMapper and the Southern Sky Survey: a valuable resource for stellar astrophysics. In *Proc. Eighth Pacific Rim Conference on Stellar Astrophysics: a Tribute to Kam-Ching Leung* Vol. 404 (eds Soonthornthum, B. et al.) 356–360 (Astronomical Society of the Pacific, 2009).
34. Alvarez, R. & Plez, B. Near-infrared narrow-band photometry of M-giant and Mira stars: models meet observations. *Astron. Astrophys.* **330**, 1109–1119 (1998).
35. Plez, B. *Turbospectrum: Code for Spectral Synthesis* (ASCL, 2012); https://ascl.net/1205.004
36. The Gaia Collaboration. The *Gaia* mission. *Astron. Astrophys.* **595**, A1 (2016).
37. Simon, J. D. Gaia proper motions and orbits of the ultrafaint Milky Way satellites. *Astrophys. J.* **863**, 89–103 (2018).
38. Dotter, A. et al. The Dartmouth Stellar Evolution Database. *Astrophys. J. Suppl. Ser.* **178**, 89–101 (2008).
39. Bertin, E. & Arnouts, S. SExtractor: software for source extraction. *Astron. Astrophys. Suppl.* **117**, 393–404 (1996).
40. Flaugher, B. et al. The Dark Energy Camera. *Astron. J.* **150**, 150–192 (2015).
41. Morganson, E. et al. The Dark Energy Survey image processing pipeline. *Publ. Astron. Soc. Pac.* **130**, 074501 (2018).
42. Kelson, D. Optimal techniques in two-dimensional spectroscopy: background subtraction for the 21st century. *Publ. Astron. Soc. Pac.* **115**, 688–699 (2003).
43. Simon, J. D. et al. Nearest neighbor: the low-mass Milky Way satellite Tucana III. *Astrophys. J.* **838**, 11–24 (2017).
44. Li, T. S. et al. Farthest neighbor: the distant Milky Way satellite Eridanus II. *Astrophys. J.* **838**, 8–22 (2017).
45. Dressler, A. IMACS: the Inamori–Magellan Areal Camera and Spectrograph on Magellan-Baade. *Publ. Astron. Soc. Pac.* **123**, 288–332 (2011).

46. Oemler, A., Clardy, K., Kelson, D., Walth, G. & Villanueva, E. *COSMOS: Carnegie Observatories System for MultiObject Spectroscopy* (ASCL, 2012); https://www.ascl.net/1705.001

47. Cooper, M. C., Newman, J. A., Davis, M., Finkbeiner, D. P. & Gerke, B. F. *spec2d: DEEP2 DEIMOS Spectral Pipeline* (ASCL, 2017); http://www.ascl.net/1203.003

48. Newman, J. A. et al. The DEEP2 Galaxy Redshift Survey: design, observations, data reduction, and redshifts. *Astrophys. J. Suppl.* **208**, 5–61 (2013).

49. Simon, J. D. & Geha, M. The kinematics of the ultrafaint Milky Way satellites: solving the missing satellite problem. *Astrophys. J.* **670**, 313–331 (2007).

50. Jofré, P. et al. Gaia FGK benchmark stars: metallicity. *Astron. Astrophys.* **564**, A133–A159 (2014).

51. Chubak, C. et al. Precise radial velocities of 2046 nearby FGKM stars and 131 standards. Preprint at https://arxiv.org/abs/1207.6212 (2012).

52. Astropy Collaboration. Astropy: a community Python package for astronomy. *Astron. Astrophys.* **558**, A33–A41 (2013).

53. Astropy Collaboration. The Astropy Project: building an open-science project and status of the v2.0 core package. *Astron. J.* **156**, 123–141 (2018).

54. Walker, M. G. et al. Internal kinematics of the Fornax dwarf spheroidal galaxy. *Astron. J.* **131**, 2114–2139 (2006).

55. Foreman-Mackey, D., Hogg, D. W., Lang, D. & Goodman, J. emcee: the MCMC hammer. *Publ. Astron. Soc. Pac.* **125**, 306–312 (2013).

56. Wolf, J. et al. Accurate masses for dispersion-supported galaxies. *Mon. Not. R. Astron. Soc.* **406**, 1220–1237 (2010).

57. Carrera, R., Pancino, E., Gallart, C. & del Pino, A. The near-infrared Ca ɪɪ triplet as a metallicity indicator—II. Extension to extremely metal-poor metallicity regimes. *Mon. Not. R. Astron. Soc.* **434**, 1681–1691 (2013).

58. Chiti, A. & Frebel, A. Four metal-poor stars in the Sagittarius dwarf spheroidal galaxy. *Astrophys. J.* **875**, 112–121 (2019).

59. Tody, D. The IRAF data reduction and analysis system. *Proc. SPIE* **0627**, 15–35 (1986).

60. Tody, D. IRAF in the nineties. In *Proc. Astronomical Data Analysis Software and Systems II* (eds Hanisch, R. J. et al.) 173–183 (Astronomical Society of the Pacific, 1993).

61. Casey, A. R. A tale of tidal tails in the Milky Way. Preprint at https://arxiv.org/abs/1405.5968 (2014).

62. Sneden, C. A. *Carbon and Nitrogen Abundances in Metal-Poor Stars*. PhD dissertation, Univ. Texas at Austin (1973).

63. Sobeck, J. S. et al. The abundances of neutron-capture species in the very metal-poor globular cluster M15: a uniform analysis of red giant branch and red horizontal branch stars. *Astron. J.* **141**, 175–192 (2011).

64. Castelli, F. & Kurucz, R. L. New grids of ATLAS9 model atmospheres. Preprint at https://arxiv.org/abs/astro-ph/0405087 (2004).

65. Kurucz, R. L. Including all the lines. *Can. J. Phys.* **89**, 417–428 (2011).

66. Sneden, C., Lawler, J. E., Cowan, J. J., Ivans, I. I. & Den Hartog, E. A. New rare earth element abundance distributions for the sun and five *r*-process-rich very metal-poor stars. *Astrophys. J. Suppl.* **182**, 80–96 (2009).

67. Sneden, C., Lucatello, S., Ram, R. S., Brooke, J. S. A. & Bernath, P. Line lists for the $A\ ^2\Pi–X\ ^2\Sigma^+$ (red) and $B\ ^2\Sigma^+–X\ ^2\Sigma^+$ (violet) systems of CN, $^{13}C^{14}N$, and $^{12}C^{15}N$, and application to astronomical spectra. *Astrophys. J. Suppl.* **214**, 26–35 (2014).

68. Sneden, C. et al. Iron-group abundances in the metal-poor main-sequence turnoff star HD 84937. *Astrophys. J.* **817**, 53–78 (2016).

69. Abbott, T. M. C. et al. The Dark Energy Survey: Data Release 1. *Astrophys. J. Suppl. Ser.* **239**, 18–42 (2018).

70. Frebel, A., Casey, A. R., Jacobson, H. R. & Yu, Q. Deriving stellar effective temperatures of metal-poor stars with the excitation potential method. *Astrophys. J.* **769**, 57–66 (2013).

71. Walker, M. G. et al. Magellan/M2FS spectroscopy of the Reticulum 2 dwarf spheroidal galaxy. *Astrophys. J.* **808**, 108–121 (2015).

72. Kirby, E. et al. Multi-element abundance measurements from medium-resolution spectra. III. Metallicity distributions of Milky Way dwarf satellite galaxies. *Astrophys. J.* **727**, 78–92 (2011).

73. Czekaj, M. A., Robin, A. C., Figueras, F., Luri, X. & Maywood, M. The Besancon Galaxy model renewed. I. Constraints on the local star formation history from Tycho data. *Astron. Astrophys.* **564**, A102–A121 (2014).

74. Moskowitz, A. G. & Walker, M. G. Stellar density profiles of dwarf galaxies. *Astrophys. J.* **892**, 27–51 (2020).

75. Kim, D., Jerjen, H., Milone, A. P., Mackey, D. & Da Costa, G. S. Discovery of a faint outer halo Milky Way star cluster in the southern sky. *Astrophys. J.* **803**, 63–71 (2015).

76. Crnojević, D. et al. Deep imaging of Eridanus II and its lone star cluster. *Astrophys. J. Lett.* **824**, L14–L19 (2016).

77. Conn, B. C., Jerjen, H., Kim, D. & Schirmer, M. On the nature of ultrafaint dwarf galaxy candidates. I. DES1, Eridanus III, and Tucana V. *Astrophys. J.* **852**, 68–86 (2018).

78. Jerjen, H., Conn, B., Kim, D. & Schirmer, M. On the nature of ultra-faint dwarf galaxy candidates. III. Horologium I, Pictor I, Grus I, and Phoenix II. Preprint at https://arxiv.org/abs/1809.02259 (2018).

79. Luque, E. et al. Deep SOAR follow-up photometry of two Milky Way outer-halo companions discovered with Dark Energy Survey. *Mon. Not. R. Astron. Soc.* **478**, 2006–2018 (2018).

80. Mutlu-Pakdil, B. et al. A deeper look at the new Milky Way satellites: Sagittarius II, Reticulum II, Phoenix II, and Tucana III. *Astrophys. J.* **863**, 25–35 (2018).

81. Vivas, A. K., Martínez-Vázquez, C. & Walker, A. R. Gaia RR Lyrae stars in nearby ultra-faint dwarf satellite galaxies. *Astrophys. J. Suppl. Ser.* **247**, 35–46 (2020).

82. Gibbons, S. L. J., Belokurov, V. & Evans, N. W. 'Skinny Milky Way please', says Sagittarius. *Mon. Not. R. Astron. Soc.* **445**, 3788–3802 (2014).

83. Erkal, D. et al. The total mass of the Large Magellanic Cloud from its perturbation on the Orphan stream. *Mon. Not. R. Astron. Soc.* **487**, 2685–2700 (2019).

84. Erkal, D. et al. Modelling the Tucana III stream—a close passage with the LMC. *Mon. Not. R. Astron. Soc.* **481**, 3148–3159 (2018).

85. McMillan, P. J. The mass distribution and gravitational potential of the Milky Way. *Mon. Not. R. Astron. Soc.* **465**, 76–94 (2017).

86. Dehnen, W. & Binney, J. Mass models of the Milky Way. *Mon. Not. R. Astron. Soc.* **294**, 429–438 (1998).

87. Hernquist, L. An analytical model for spherical galaxies and bulges. *Astrophys. J.* **356**, 359–364 (1990).

88. Pace, A. B. & Li, T. S. Proper motions of Milky Way ultra-faint satellites with Gaia DR2 × DES DR1. *Astrophys. J.* **875**, 77–92 (2019).

89. Kallivayalil, N., van der Marel, R. P., Besla, G., Anderson, J. & Alcock, C. Third-epoch Magellanic Cloud proper motions. I. *Hubble Space Telescope*/WFC3 data and orbit implications. *Astrophys. J.* **764**, 161–184 (2013).

90. van der Marel, R. P., Alves, D. R., Hardy, E. & Suntzeff, N. B. New understanding of Large Magellanic Cloud structure, dynamics, and orbit from carbon star kinematics. *Astron. J.* **124**, 2639–2663 (2002).

91. Pietrzyński, G. et al. An eclipsing-binary distance to the Large Magellanic Cloud accurate to two per cent. *Nature* **495**, 76–79 (2013).

92. Bovy, J. galpy: a Python library for galactic dynamics. *Astrophys. J. Suppl. Ser.* **216**, 29–55 (2014).

93. Webb, J. J., Bovy, J., Carlberg, R. G. & Gieles, M. Modelling the effects of dark matter substructure on globular cluster evolution with the tidal approximation. *Mon. Not. R. Astron. Soc.* **488**, 5748–5762 (2019).

94. Read, J. I. & Steger, P. How to break the density–anisotropy degeneracy in spherical stellar systems. *Mon. Not. R. Astron. Soc.* **471**, 4541–4558 (2017).

95. Binney, J. & Mamon, G. A. *M/L* and velocity anisotropy from observations of spherical galaxies, or must M87 have a massive black hole? *Mon. Not. R. Astron. Soc.* **200**, 361–375 (1982).

96. Binney, J. & Tremaine, S. *Galactic Dynamics* 2nd edn (Princeton Univ. Press, 2008).

97. Chang, L. & Necib, L. Dark matter density profiles in dwarf galaxies: linking Jeans modeling systematics and observation. Preprint at https://arxiv.org/abs/2009.00613 (2020).

98. Navarro, J., Frenk, C. S. & White, S. D. M. A universal density profile from hierarchical clustering. *Astrophys. J.* **490**, 493–508 (1997).

99. Bonnivard, V., Maurin, D. & Walker, M. G. Contamination of stellar-kinematic samples and uncertainty about dark matter annihilation profiles in ultrafaint dwarf galaxies: the example of Segue I. *Mon. Not. R. Astron. Soc.* **462**, 223–234 (2016).

100. Osipkov, L. P. Spherical systems of gravitating bodies with an ellipsoidal velocity distribution. *Sov. Astron. Lett.* **5**, 42–44 (1979).

101. Merritt, D. Spherical stellar systems with spheroidal velocity distributions. *Astron. J.* **90**, 1027–1037 (1985).

102. Hearin, A. et al. Forward modeling of large-scale structure: an open-source approach with Halotools. *Astron. J.* **154**, 190–198 (2017).

103. Dutton, A. A. & Maccio, A. V. Cold dark matter haloes in the Planck era: evolution of structural parameters for Einasto and NFW profiles. *Mon. Not. R. Astron. Soc.* **441**, 3359–3374 (2014).

104. Dotter, A. MESA Isochrones and Stellar Tracks (MIST) 0: methods for the construction of stellar isochrones. *Astrophys. J. Suppl. Ser.* **222**, 8–18 (2016).

105. Choi, J. et al. MESA Isochrones and Stellar Tracks (MIST). I. Solar-scaled models. *Astrophys. J.* **823**, 102–149 (2016).

106. Paxton, B. et al. Modules for Experiments in Stellar Astrophysics (MESA). *Astrophys. J. Suppl.* **192**, 3–37 (2011).

107. Paxton, B. et al. Modules for Experiments in Stellar Astrophysics (MESA): planets, oscillations, rotation, and massive stars. *Astrophys. J. Suppl.* **208**, 4–45 (2013).

108. Paxton, B. et al. Modules for Experiments in Stellar Astrophysics (MESA): binaries, pulsations, and explosions. *Astrophys. J. Suppl. Ser.* **220**, 15–58 (2015).

109. Bressan, A. et al. PARSEC: stellar tracks and isochrones with the PAdova and TRieste Stellar Evolution Code. *Mon. Not. R. Astron. Soc.* **427**, 127–145 (2012).
110. Chen, Y. et al. Improving PARSEC models for very low mass stars. *Mon. Not. R. Astron. Soc.* **444**, 2525–2543 (2014).
111. Tang, J. et al. New PARSEC evolutionary tracks of massive stars at low metallicity: testing canonical stellar evolution in nearby star-forming dwarf galaxies. *Mon. Not. R. Astron. Soc.* **445**, 4287–4305 (2014).
112. Chen, Y. et al. PARSEC evolutionary tracks of massive stars up to 350 $M_\odot$ at metallicities $0.0001 \leq Z \leq 0.04$. *Mon. Not. R. Astron. Soc.* **453**, 1068–1080 (2015).
113. Marigo, P. et al. A new generation of PARSEC-COLIBRI stellar isochrones including the TP-AGB phase. *Astrophys. J.* **835**, 77–95 (2017).
114. Pastorelli, G. et al. Constraining the thermally pulsing asymptotic giant branch phase with resolved stellar populations in the Small Magellanic Cloud. *Mon. Not. R. Astron. Soc.* **485**, 5666–5692 (2019).

Author contributions

A.C. selected candidates for the observations, made the observations and led the analysis and paper writing; A.F. assisted with the MagE observations and subsequent analysis and J.D.S. assisted with the IMACS observations and subsequent analysis; H.J., D.K. and J.E.N. provided the SkyMapper images from which targets were selected; D.E. modelled the orbit of Tucana II; L.J.C. and L.N. modelled the extended density profile of Tucana II; A.P.J. contributed to the analysis of the MagE spectra; all authors contributed to the interpretation of the data, and contributed to writing the paper or provided feedback.

Competing interests

The authors declare no competing interests.

Additional information

Extended data is available for this paper at https://doi.org/10.1038/s41550-020-01285-w.

Supplementary Information The online version contains supplementary material available at https://doi.org/10.1038/s41550-020-01285-w.

Correspondence and requests for materials should be addressed to A.C.

Peer review information *Nature Astronomy* thanks Quinn Minor and the other, anonymous, reviewer(s) for their contribution to the peer review of this work.

Reprints and permissions information is available at www.nature.com/reprints.

Publisher's note Springer Nature remains neutral with regard to jurisdictional claims in published maps and institutional affiliations.
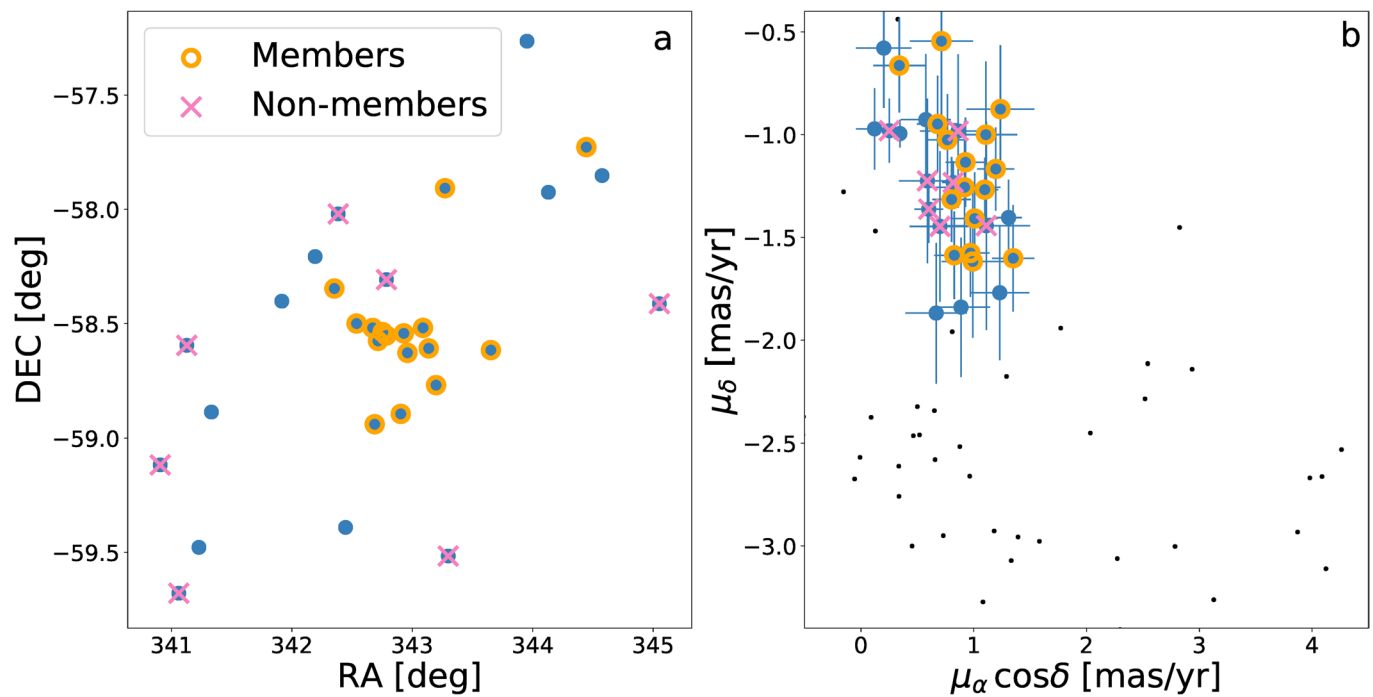
Extended Data Fig. 1 | Identification of candidate members of Tucana II. a. Locations of candidate members (blue data points) with g < 19.5. Candidates were selected by identifying metal-poor giants with SkyMapper photometry (photometric [Fe/H] < −1.0 and photometric log g < 3.0 ref. [21]), and then only including stars with proper motions around the systemic proper motion of Tucana II (0.2 mas/yr < $\mu_\alpha \cos\delta$ < 1.4 mas/yr and −1.7 mas/yr < μ_δ < −0.5 mas/yr). All stars confirmed as members of Tucana II in this work or prior work[15,17] are highlighted in orange. Confirmed non-members of Tucana II that were observed in this work are marked in magenta. **b**. Proper motions of candidate members with g < 19.5. The notation of the data points is equivalent to that in panel a. The majority of stars with proper motions near the systemic proper motion of Tucana II are members. This results from our exclusion of stars that are not metal-poor giants using log g to cut out foreground stars. Milky Way foreground stars outside our proper motion selection criteria are shown as small black points. The error bars on the proper motions correspond to 1sigma uncertainties in the *Gaia* DR2 catalog.
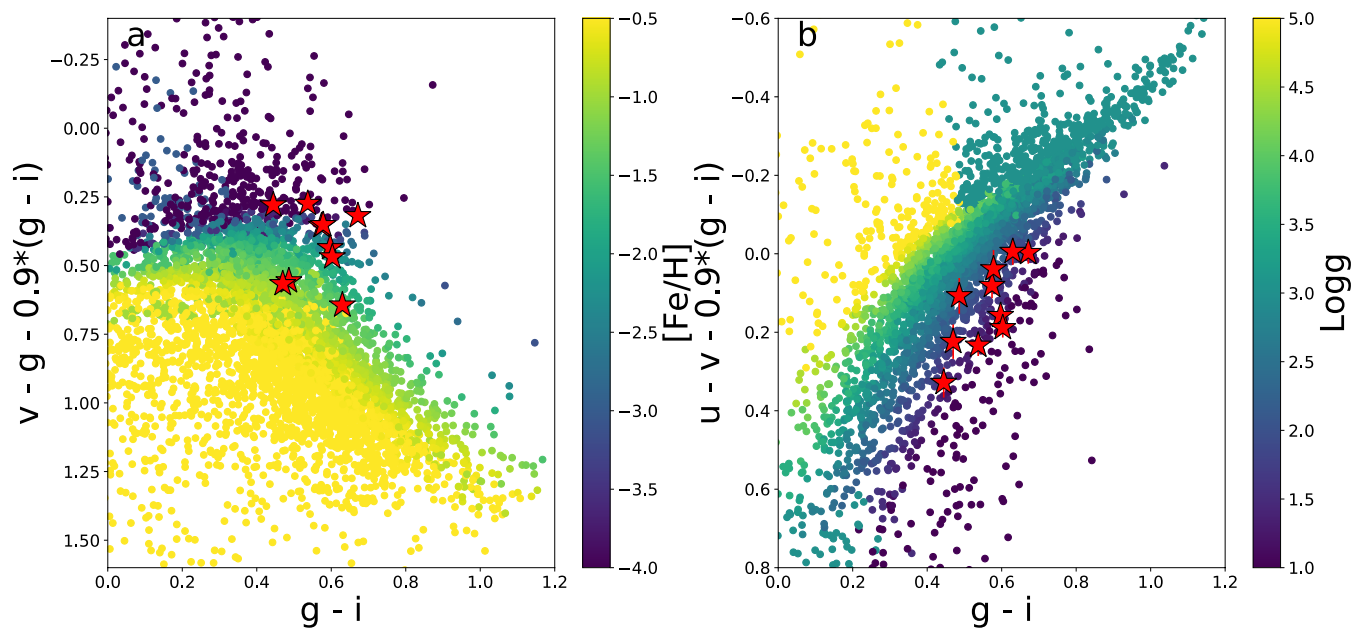
Extended Data Fig. 2 | SkyMapper photometry of Tucana II members observed with MagE. a. A metallicity-sensitive SkyMapper color-color plot of every star within a degree of Tucana II. The Tucana II members observed with MagE in this study are shown as red stars, and all have photometric [Fe/H] < -1.0. Photometric metallicities were derived following ref. [21], and are indicated by the color scale. The magnitudes are in the AB magnitude system. **b**. A surface gravity-sensitive SkyMapper color-color plot of every star within a degree of Tucana II. Similarly to the metallicity-sensitive plot, the Tucana II members observed with MagE separate from the foreground population due to their low surface gravities. The surface gravities are indicated by the color scale. Magnitudes are in the AB magnitude system.
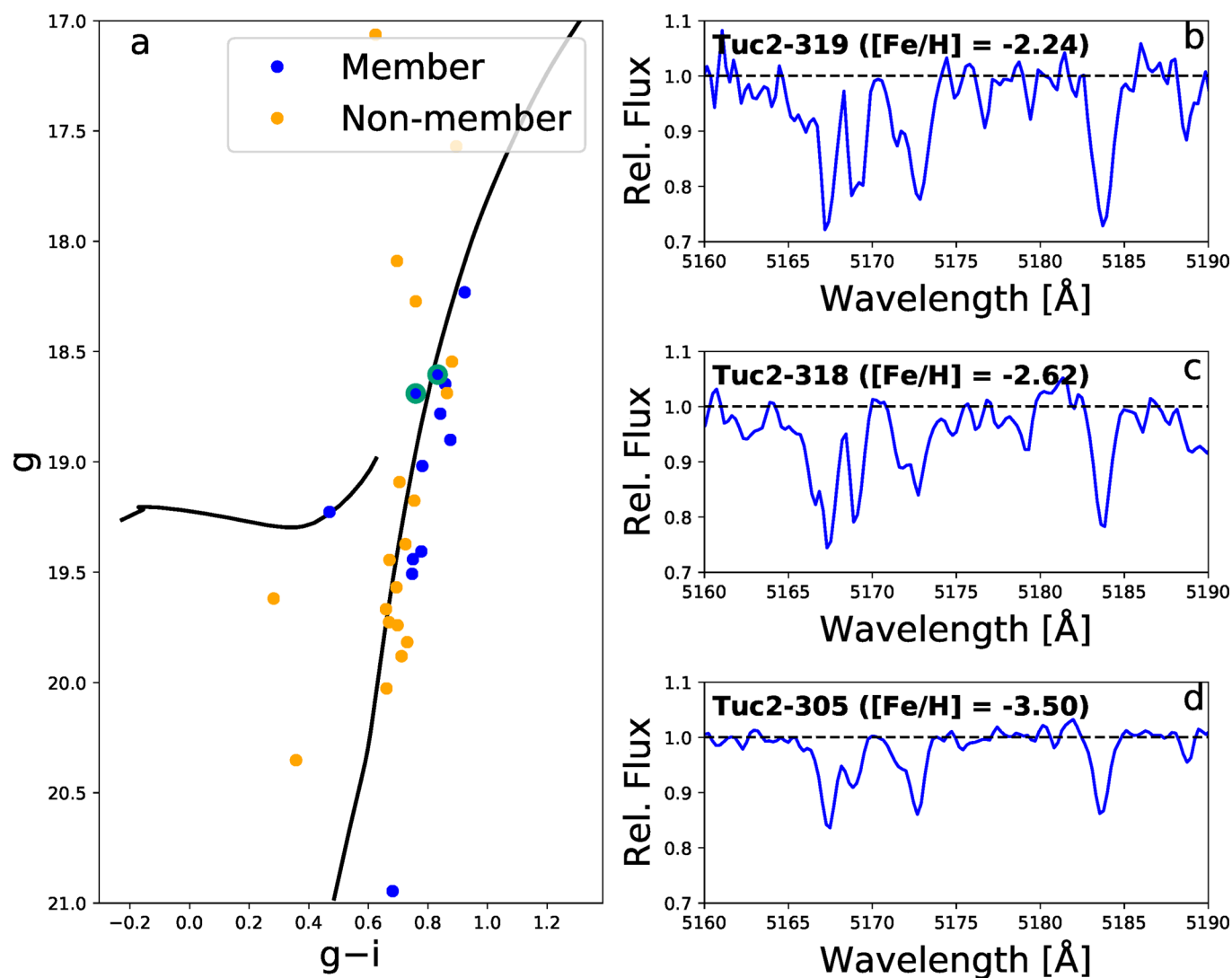
Extended Data Fig. 3 | Color-magnitude diagram of Tucana II and sample spectra. a. Color-magnitude diagram of the MagE and IMACS Tucana II members with DES photometry. A 10 Gyr, [Fe/H] = -2.2 MIST isochrone[104–108] at the distance modulus of Tucana II[18] is overplotted for reference. The horizontal branch from a PARSEC isochrone[109–114] with the same parameters is also shown. Members and non-members are indicated in blue and orange, respectively. The two most distant members are outlined in pink. Magnitudes are in the AB magnitude system. **b–d**. MagE spectra of the magnesium region Tuc2-319, Tuc2-318, and Tuc2-305. The absorption lines in the region become noticeably weaker at lower metallicities. A dashed horizontal line is drawn at the continuum level to guide the eye.
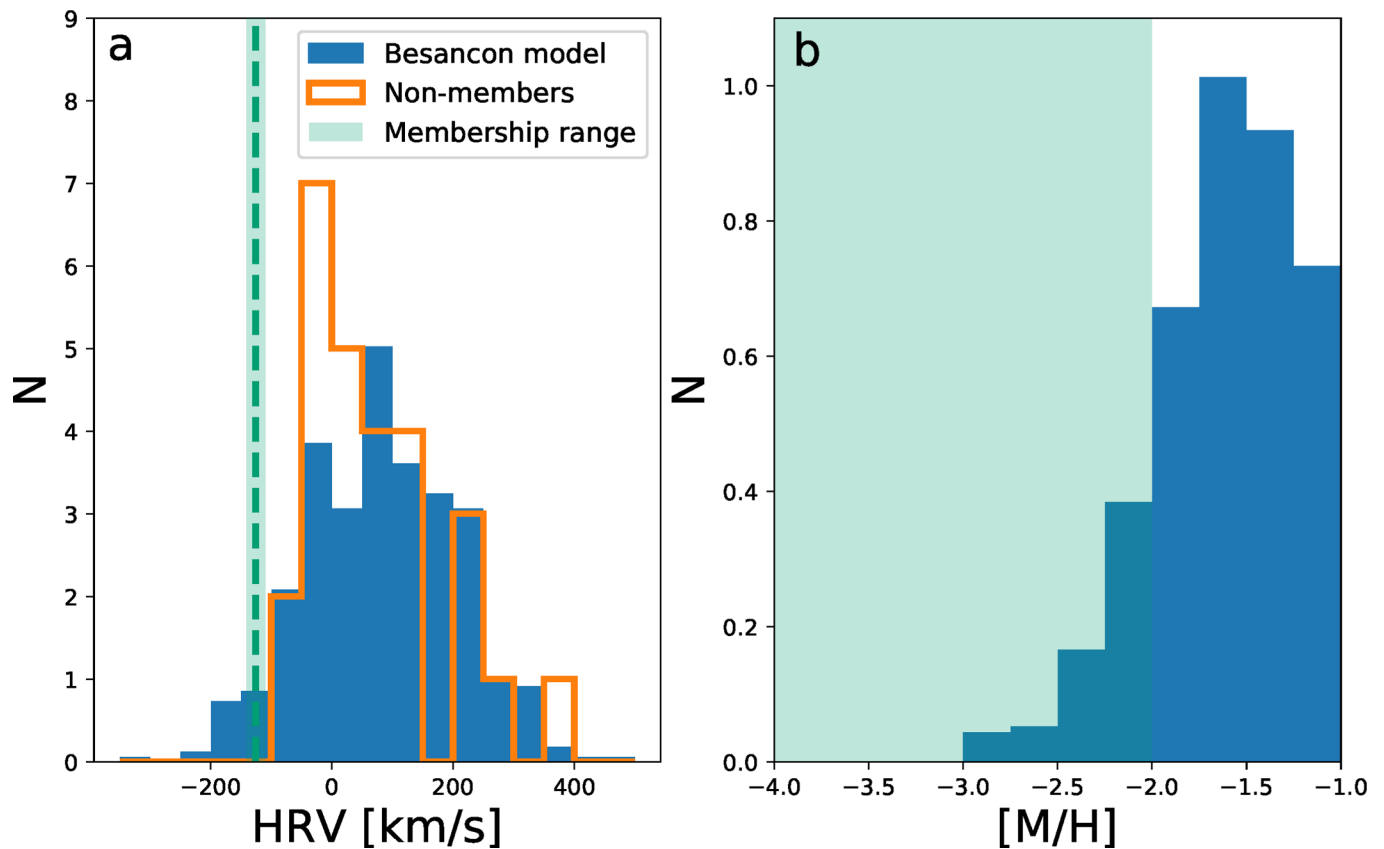
Extended Data Fig. 4 | Comparison of Tucana II radial velocities and metallicities to simulated radial velocities and metallicities of foreground stars.
a. A histogram of MagE and IMACS radial velocities of stars determined to be non-members of Tucana II is shown in orange. In blue, we plot a scaled histogram of radial velocities of stars in the field of Tucana II, as generated from the Besancon model of stellar populations in the galaxy[72] after replicating our target selection cuts (blue). The vertical red line marks the systemic velocity of Tucana II[15] and the green shaded region corresponds to our Tucana II velocity membership criteria ($-141\,$km/s $<$ HRV $< -110\,$km/s; [Fe/H] < -2.0), which is well separated from the foreground velocity distribution. **b**. Scaled histogram of metallicities of stars generated from the Besancon model following those in panel a. The green shaded region ([Fe/H] < -2.0) corresponds to the metallicities of the newly detected Tucana II members. Only 0.4% of simulated foreground stars satisfy our Tucana II velocity and metallicity membership criteria ($-141\,$km/s $<$ HRV $< -110\,$km/s; [Fe/H] < -2.0).